Contents lists available at ScienceDirect

International Journal of Refractory Metals and Hard Materials

Dense nanocrystalline W alloys: Enhancement of hardness and thermal stability by Al addition

Francesco Torre [a],[1], Teodor Huminiuc [b], Paolo Barra [a], Luciano Pilloni [c], Tomas Polcar [b], Antonio Rinaldi [c], Francesco Delogu [a],[d],[e], Roberto Orrù [a],[d],[e], Giacomo Cao [a],[d],[e], Antonio Mario Locci [a],[d],[e],*

[a] *Dipartimento di Ingegneria Meccanica, Chimica e dei Materiali, Università degli Studi di Cagliari, Via Marengo 3, 09123 Cagliari, Italy*
[b] *Engineering Materials, Faculty of Engineering and Physical Sciences, University of Southampton, Southampton SO17 1BJ, United Kingdom*
[c] *Sustainability Department, SSPT-PROMAS-MATPRO, ENEA, Via Anguillarese 301, Roma, Italy*
[d] *Consorzio Interuniversitario per lo Sviluppo dei Sistemi a Grande Interfase (CSGI), via della Lastruccia 3, 50019 Sesto Fiorentino, Italy*
[e] *Cagliari Research Unit, via Marengo 2, 09123 Cagliari, Italy*

ARTICLE INFO

ABSTRACT

Nanocrystalline $W_{100-x}Al_x$ (x up to 20 at.%) powders obtained by mechanical alloying have been consolidated by spark plasma sintering (SPS). Alloying W with Al significantly improves the sinterability, allowing the fabrication of dense samples. The consolidation process keeps the nanocrystalline microstructure substantially unaffected, which contributes to the hardness of the final W-Al alloys. The room-temperature nano- and micro-hardness of dense $W_{80}Al_{20}$ alloy sintered at 1100 °C are as high as 18 and 14 GPa, respectively. These values are significantly higher than those previously reported for pure coarse- or submicron-grained W and may be ultimately ascribed to the grain boundary segregation of Al.

1. Introduction

In the past decade, W and its alloys have become a specific focus of scientific research in materials science. With their high melting point, significant corrosion and wear resistance, high density and good strength at high temperature, W-based alloys are generally regarded as high-temperature structural materials with relevant possible application in aerospace, nuclear and chemical industries [1–6]. However, the excellent high-temperature properties are associated with unsatisfactory plastic processing capabilities. Room-temperature brittleness and hardness seriously undermine workability, which makes the manufacturing of complex parts definitely challenging.

In this regard, alloying W with Al is generally expected to be beneficial. Low melting point, soft Al can enhance the W plastic properties and improve its sinterability, thus facilitating the forming of parts with complex shapes. In addition, the grain boundary (GB) segregation of Al in W-Al alloys can impart a thermodynamic stabilization to the material microstructure [7], enabling the preservation of the nanocrystalline

structure under severe processing and working conditions. In spite of this, W-Al alloys have, so far, received scarce attention. This can be reasonably ascribed to the huge difference between Al and W in terms, for instance, of melting points, density and plasticity. Alloying the two elements by conventional melting-based processes is impracticable.

Starting from the beginning of 2000s, such problem has been overcome by using mechanical alloying (MA), which allowed obtaining W-Al alloys in powder form [8–13]. In most cases, MA was carried out in planetary ball mills with very high ball-to-powder mass ratio (BPR) and W-Al powder mixtures with relatively large Al content. These processing conditions clearly mirror the difficulty of obtaining homogeneous chemically disordered solid solutions of Al in W when the Al content is low, since the difference in plasticity and hardness between the two elemental species slows down the forced atomic-scale mixing induced by the mechanical processing.

Nevertheless, in previous work [7] we have shown that the use of a relatively high-energy ball mill enables the formation of the desired nanocrystalline solid solution at much lower BPRs. Using a ball mill with
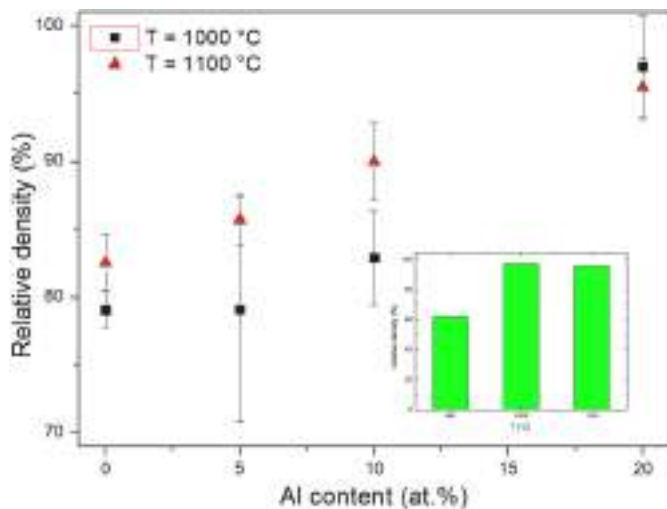

Fig. 1. Relative density of samples sintered by SPS as a function of aluminum content. Inset shows relative densities of W-20 at.% Al as function of sintering temperature.
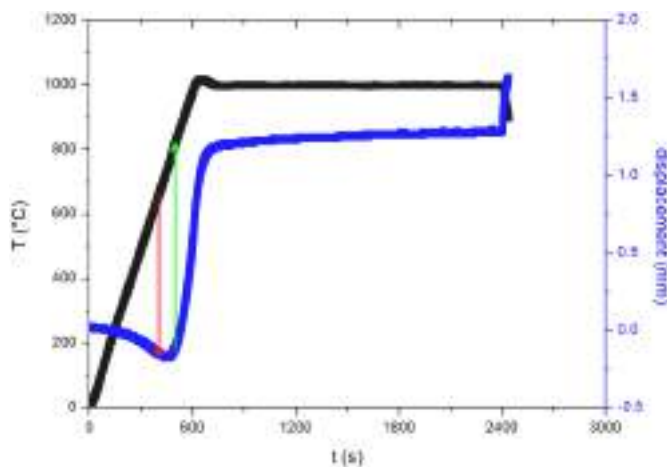

Fig. 2. Temperature time profile (black curve) imposed to the ensemble and displacement (blue curve) of the upper electrode of the SPS apparatus during consolidation of W-20 at.% Al at 1000 °C. (For interpretation of the references to colour in this figure legend, the reader is referred to the web version of this article.)

an effective agitation of powders and balls results, indeed, in more effective impacts and, consequently, in a faster forced mixing of the atomic species on the microscopic scale. Within the same context, we also proved that the nanocrystalline structure of the W-Al alloys fabricated by MA exhibits enhanced stability compared with pure nanocrystalline W, being the initial grain size and the annealing conditions the same [7]. Such evidence leaves room to further developments regarding the compaction of W-Al alloy powders by technologically relevant forming processes and raises questions concerning the stability of the nanocrystalline structure of W-Al alloys under the severe processing conditions such processes involve.

In the present work, we aim at providing a clear response to such questions and, simultaneously, proving the feasibility of powder densification processes capable to leave the properties of nanocrystalline W-Al alloys unaffected. To this aim, we fabricated nanocrystalline W-Al alloys with Al molar fraction between 0 and 0.2 by MA using a BPR as low as 1.6. Then, we compacted the powders by spark plasma sintering (SPS). Utilizing uniaxial compression and pulsed direct electrical currents, SPS allows performing high-speed consolidation processes under

definitely severe conditions. The passage of electrical current across the conductive powder results in very high heating and cooling rates, thus favoring densification processes over grain growth ones.

We show that, despite the severe processing conditions, we are able to fabricate fully dense W-Al alloys with nanocrystalline structure. The average grain size is weakly affected by local temperature rises and the powders of the W-Al alloys are much more workable than pure W ones. We also show that the processing conditions do not alter the distribution of Al atoms in the nanocrystalline structure, preserving the Al segregation at W GBs that we identify as the main factor underlying the relative stability of the nanocrystalline structure and the hardness of the W-Al alloys we obtained.

In the following, we provide full detail regarding the experimental methodologies, the fabrication of dense nanostructure samples by SPS, characterization of structural and microstructural properties, and the results of micromechanical testing.

2. Materials and methods

2.1. Mechanical alloying

Nanocrystalline W-Al alloy powders with 5, 10, and 20 at.% of aluminum were produced by mechanical alloying (MA) using a SPEX Mixer/Mill 8000 (SPEX CertiPrep, USA). High purity (99.99%) commercial W and Al powders were initially mixed according to the desired molar ratio. Pure W was also processed as a reference. A total amount of 15 g of powder was sealed in a cylindrical steel vial with three steel balls of 8 g each. Powders were handled inside a glove box under an inert Ar atmosphere with moisture and oxygen content below 5 ppm to avoid undesired oxidation processes. Mechanical treatments of different duration were then performed under Ar atmosphere. Each time, the vial was emptied and refilled with a new charge of powders. Additional experimental details can be found elsewhere [11].

2.2. Spark plasma sintering

W-Al alloy powders obtained by MA were consolidated using an SPS 515 apparatus (Fuji Electronic Industrial Co., Kanagawa, Japan). About 4 g of powders were inserted in a cylindrical graphite die with an internal diameter of 10 mm, and symmetrically closed with graphite plungers measuring 22 mm in height and 9.5 mm in diameter. Densification was performed at 900 °C, 1000 °C, and 1100 °C using a heating rate of 100 °C/min and maintaining the dwell temperature for 30 min. During the heating step, the applied mechanical load was gradually increased up to 6.3 kN and subsequently kept constant during the isothermal step, ensuring a pressure of about 80 MPa. The obtained pellets, which were about 3.5 mm high and 9.5 mm in diameter, were grinded to remove graphite residues. Finally, Archimedes' density was measured.

2.3. Characterization

2.3.1. X-ray diffraction (XRD)

MAed powders and SPSed samples were examined using a Rigaku Miniflex II diffractometer equipped with Cu K_α radiation ($\lambda = 1.5405$ Å). XRD patterns were collected over a scattering angle range from 10 to 140°. The obtained XRD patterns were analyzed according to the Rietveld method using the Maud software [14].

2.3.2. Scanning electron microscopy (SEM)

Samples microstructure was investigated by SEM, using a LEO 1530 (Zeiss, Oberkochen, Germany) instrument equipped with a high-resolution in-lens secondary electron detector, a conventional secondary electron detector, a Centaurus backscattered detector and an XACT microanalysis unit (OXFORD Instruments, Abingdon, United Kingdom).
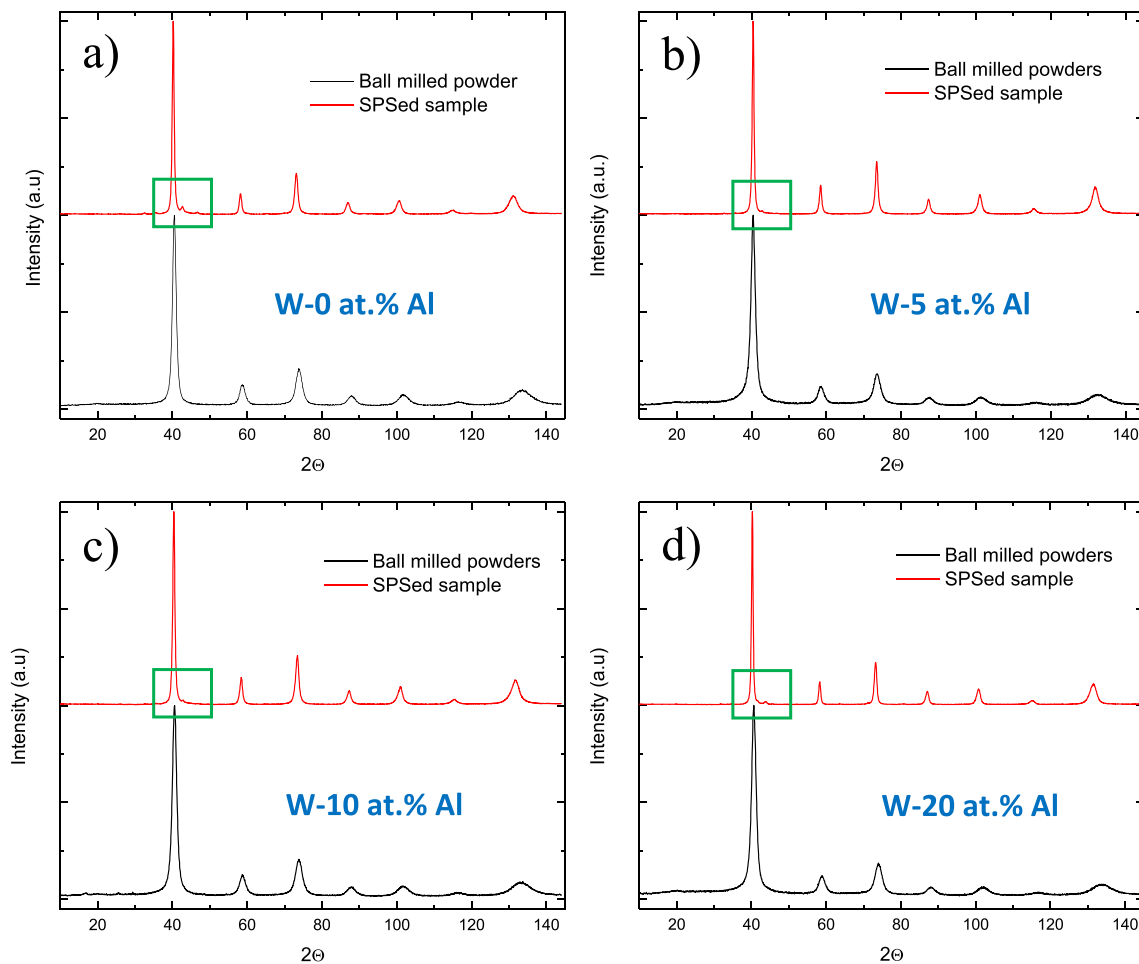
Fig. 3. XRD patterns of ball milled powder (black lines) and SPSed samples (red lines): a) W- 0 at.% Al; b) W- 5 at.% Al; c) W- 10 at.% Al; d) W- 20 at.% Al. Green boxes highlight patterns range where peaks of secondary phases may appear. (For interpretation of the references to colour in this figure legend, the reader is referred to the web version of this article.)
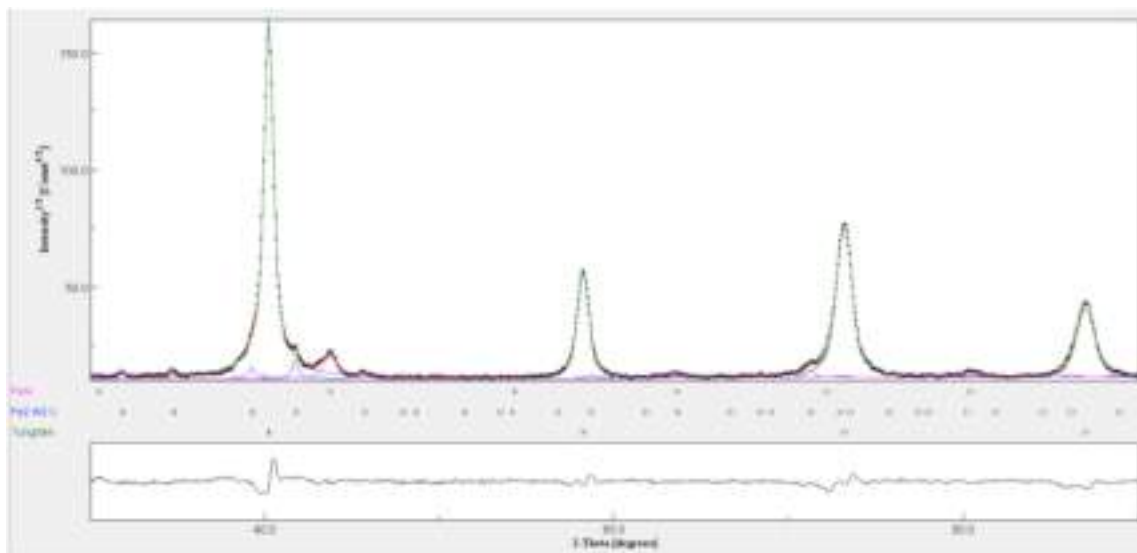

Fig. 4. XRD pattern of the $W_{80}Al_{20}$ sample sintered at 1000 °C along with the best-fitted Rietveld profile.

2.3.3. Transmission electron microscopy (TEM)

Micrographs and chemical maps were obtained using a JEOL ARM 200F (STEM) and FEI Titan3 (TEM and STEM) electron microscopes equipped with a probe and image aberration corrector and operating in mode at 200 kV and 300 kV acceleration voltage, respectively. A Thermo Scientific EDS detector was used for the acquisition of chemical maps,
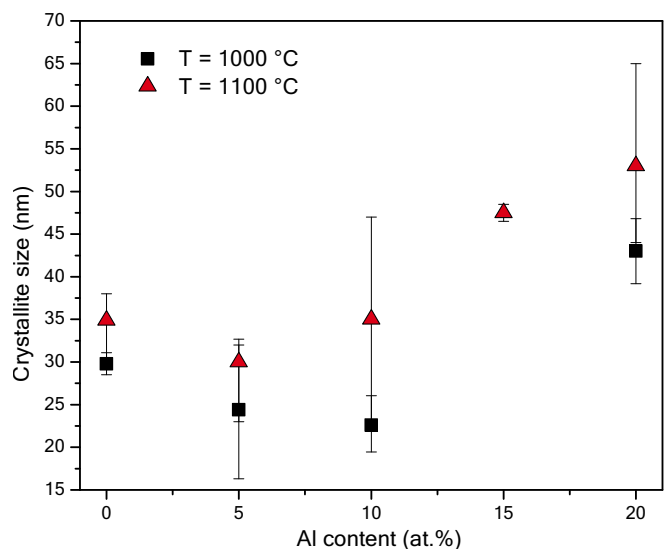
Fig. 5. Average coherent diffraction domain (crystallite size) of SPS sintered samples as a function of Al content.

which were summed over 100 frames for the improvement of the signal-to-noise ratio (SNR). Selected area electron diffraction (SAED) was also performed.

2.3.4. Mechanical testing

Microhardness was measured by means of a ZwickRoell micro-indenter equipped with a diamond Vickers tip. Measurements were performed by applying a 500 g load at a speed of 0.45 N/s, dwell time of 12 s, and load removal speed of 20 mm/min. For each sample, a total of 5 indentations were performed. Nanoindentation experiments were carried out by means of a MicroMaterials NanoTest Vantage indenter equipped with a diamond Berkovich tip. For each sample, a total of 30 indentations were performed, using a load of 300 mN, a loading rate of 0.5 mN/s, and an unloading rate of 0.2 mN/s. Hardness and elastic modulus were estimated according to the Oliver-Pharr method [15].

3. Results and discussion

3.1. Spark plasma sintering

Nanocrystalline W and W-Al alloy powders obtained by mechanical alloying, whose characteristics will be discussed afterwards, were consolidated to investigate the effect of Al addition on the density, grain
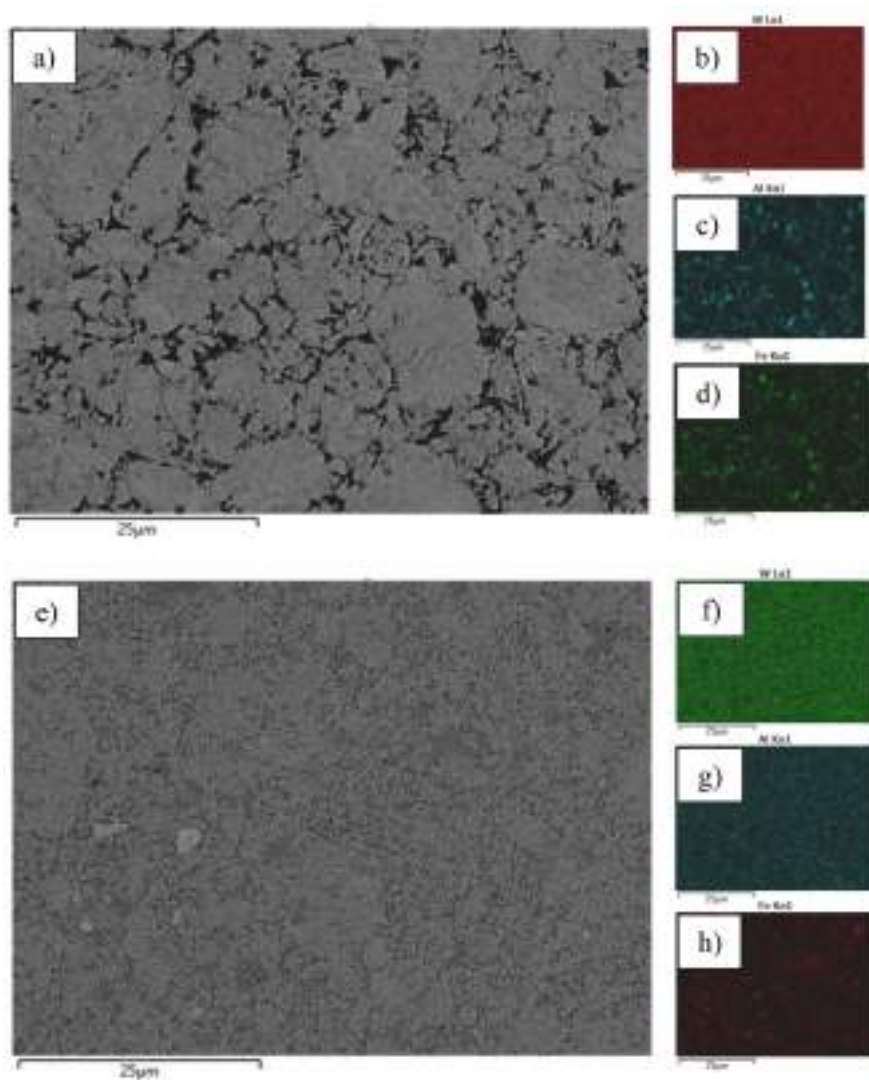

Fig. 6. SEM images of $W_{80}Al_{20}$ samples sintered at 1000 °C (figure a)) and 1100 °C (figure e)). Corresponding chemical analysis are reported in figures b)-d) (T=1000 °C) and figures f)-h) (T=1100 °C).
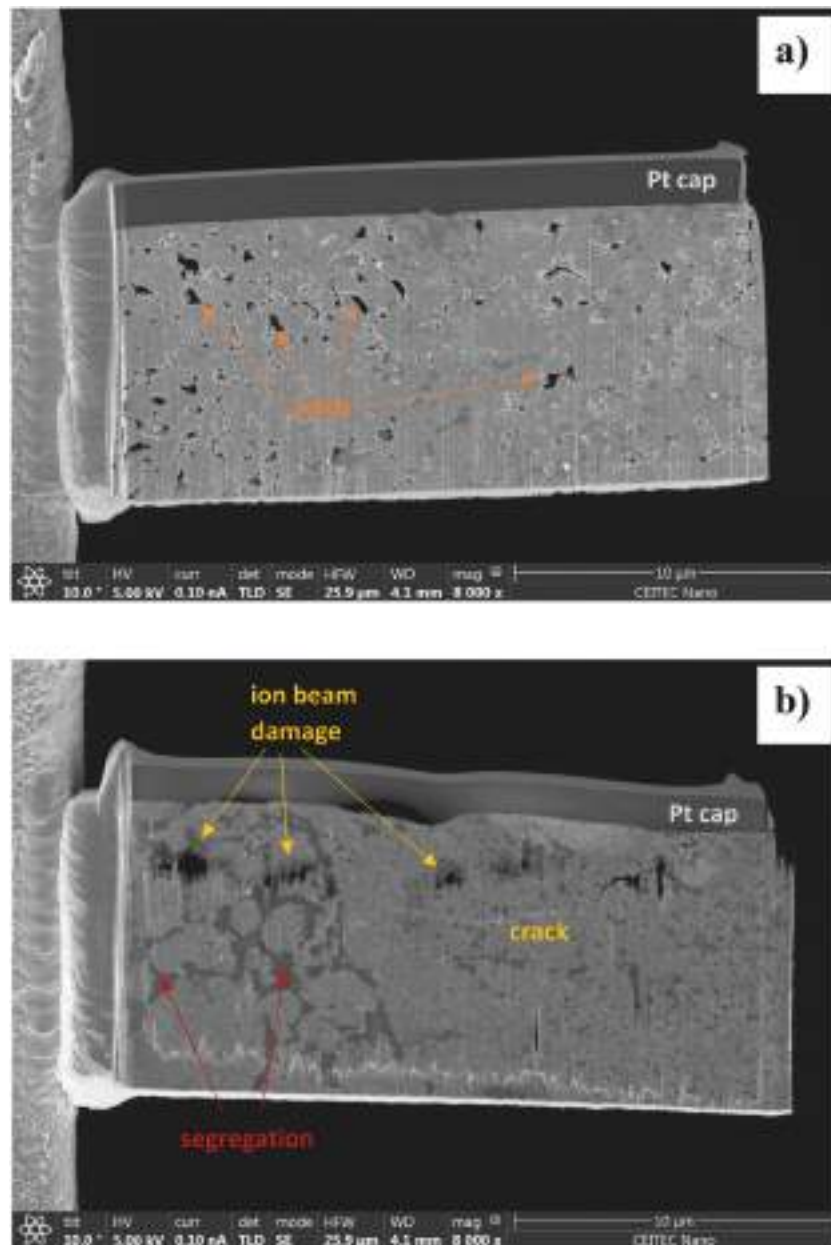
Fig. 7. SEM images of the TEM lamellae of samples sintered at 1000 °C that were lifted for high resolution imaging: a) $W_{90}Al_{10}$; b) $W_{80}Al_{20}$.

size, microstructural features, and hardness of these materials in dense form. Powder samples of different stoichiometries were sintered at a temperature of 900–1100 °C. The effect of Al content on sample density (ρ_{rel}) is reported in Fig. 1. A progressive increase in density can be observed as the amount of aluminum in the alloy increases. Indeed, while the values of ρ_{rel} of about 80% are obtained for pure W, densities close to the theoretical one are achieved for solid solutions with Al content of 20 at.%. An increase in density can be generally observed for powders sintered at 1100 °C compared to samples consolidated at 1000 °C. However, such increases become less significant with an increasing amount of Al, as observed in the inset of Fig. 1, for the case of W-20 at.% Al system. Indeed, it can be seen a significant increase of the relative density as the temperature increase from 900 °C to 1000 °C; a further increase to 1100 °C did not affect the final sample density.

It should be emphasized that the densification enhancement corresponding to an increase in the amount of Al in the alloy cannot be interpreted in the framework of liquid phase-aided sintering. Indeed, although the sintering temperature is higher than the Al melting point,

the thorough investigation performed by some of the authors, reported elsewhere [11], allowed to rule out the presence of elemental aluminum in the milled powders. It was therein shown that Al is completely dissolved in the BCC lattice structure of W. This finding can be confirmed by Fig. 2, which shows the imposed temperature time profile (black curve) along with the displacement (blue curve) of the upper electrode of the SPS apparatus. The latter quantity represents the densification evolution, since it is correlated to the sample thickness shrinkage. It is well known that the formation of a liquid phase during electric current assisted sintering gives rise to an abrupt increase in displacement [16,17].

On the contrary, such a phenomenon does not appear in Fig. 2. Moreover, we can see (red arrow) that when the system reaches the melting point of aluminum, the displacement is still decreasing due to the ensemble thermal expansion, which counteracts the still negligible densification process. Note that when sample consolidation begins (green arrow), the temperature is already above 800 °C.
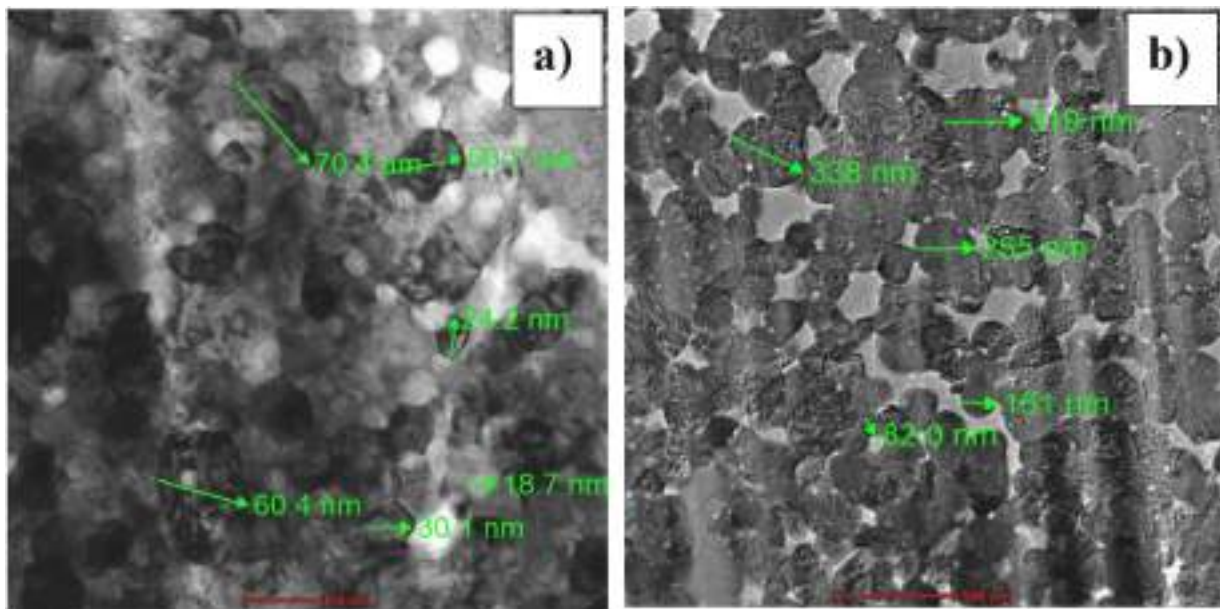
Fig. 8. TEM images of the SPSed materials: a) $W_{90}Al_{10}$; b) $W_{80}Al_{20}$.

3.2. Structural characterization

Fig. 3 shows XRD patterns of sintered samples along with those of the starting ball milled powders, for comparison purposes. Peak narrowing can be observed after SPS due to the increase in crystallite size and strain releases occurring during the consolidation process. In all cases, the XRD patterns highlight the presence of a W-based BCC solid solution, according to the initial powders composition. Instead, W-Al intermetallic compounds or free elemental Al were not detected. A closer inspection of the pattern regions enclosed by the green boxes in Fig. 3 shows the presence of small amounts of secondary phases due to Fe and C contamination coming from milling media and sintering tools, respectively. For further insight, Fig. 4 reports the XRD pattern related to the cross section of the $W_{80}Al_{20}$ sample sintered at 1000 °C, along with the best-fitted Rietveld profile. The deconvolution of the XRD peaks allows us to better appreciate the contribution of the different phases. Along with BCC W-Al (93.3 wt%), smaller amounts of Fe_2W_2C (≈ 1.5 wt%) and BCC FeAl (≈ 5.2 wt%) were identified as secondary phases.

The average coherent diffraction domain values, L, of sintered samples with different composition are reported in Fig. 5. As the Al content is increased, L does not vary monotonically. A small addition of Al (5 at.%) leads to a slightly decrease in the L value compared to the base case of pure W. Higher alloy aluminum content in the alloy resulted in larger crystallite sizes. Moreover, a coarsening trend is observed when the sintering temperature was increased from 1000 to 1100 °C. Nevertheless, nanostructure was retained in all samples, being the maximum crystallite size value in the range of 40–70 nm, for the case of $W_{80}Al_{20}$ solid solution.

The non-monotonic behavior of crystallite size as a function of the Al content in the alloys can be explained on the basis of the following reasoning. First, it should be considered that the melting temperature of the alloy decreases as Al fraction increases [18]. Therefore, although the sintering temperature is the same for all investigated alloys, the homologous temperature increases with the content of Al. In parallel, sintering (cf. Fig. 1) and grain growth rates are then expected to be enhanced. Accordingly, a positive correlation between Al content and grain size should be observed. However, it was recently found for W-Al alloys that aluminum can segregate at the grain boundaries and thermodynamically limits grain growth [7]. The competition between these two opposite effects deriving from Al addition gives rise to the results reported in Fig. 5. Indeed, when small amounts aluminum are added, the beneficial effect of its segregation at GBs exceeds the tendency to faster grain growth due to the alloy homologous temperature increase. Conversely, GB segregation of aluminum can only limit grain growth when Al content is further raised since coarsening is now greatly enhanced by the higher homologous temperature experienced by the alloys.

Sintered samples were also characterized by SEM. As an example, images of the $W_{80}Al_{20}$ alloy sintered at 1000 °C and 1100 °C are reported in Fig. 6. In the first place, the SEM observation does not evidence an excessive residual porosity, which is in line with the high densities measured for these samples (cf. Fig. 1). These micrographs show a heterogeneous microstructure with contrasting areas, which highlights the presence of secondary phases (darker areas) with different electron density compared to the main W-based solid solution (light regions). This is confirmed by the EDX chemical maps of the selected areas reported in the same figure. Overall, the samples show homogeneous solubilization of Al on the W BCC lattice, together with Fe contamination coming from the milling tools. Independently from alloy composition and sintering temperature, a tendency of Fe to form separated islands was observed. This phenomenon is much more apparent in the case of the $W_{80}Al_{20}$ sample sintered at 1000 °C, whose chemical map is shown in Fig. 6b)-d). It can be seen the formation of Fe-Al rich islands, with the rest of Al homogeneously distributed in the W matrix. XRD analysis reported in Fig. 4 identifies these islands as the intermetallics FeAl.

TEM analysis of $W_{90}Al_{10}$ and $W_{80}Al_{20}$ alloys sintered at 1000 °C was also performed. The specimen examination confirms the major differences between the two samples, namely: the density (cf. Fig. 1) and the microstructure of the material (cf. Fig. 6). Specifically, Fig. 7 shows SEM images of the TEM lamellae which were lifted for high resolution imaging. The $W_{90}Al_{10}$ sample shows the presence of voids, meaning that the material is not fully dense. Moreover, some separation of different phases is visible, but the islands are not significant in size. By comparison, $W_{80}Al_{20}$ shows a more pronounced formation of secondary phases on the left half of the specimen and a microstructure indicating near-full density.

Fig. 8 shows a comparison between the two sintered materials microstructures. A clear difference is given by the average grain size, which appears higher by a factor of 2 to 3 for the $W_{80}Al_{20}$ sample. The lower Al content sample has an average grain size of about 50 nm, whereas grains up to 150–200 nm sized can be seen for the case of $W_{80}Al_{20}$ alloy. The observed nanostructures are comparable with the result of the Rietveld
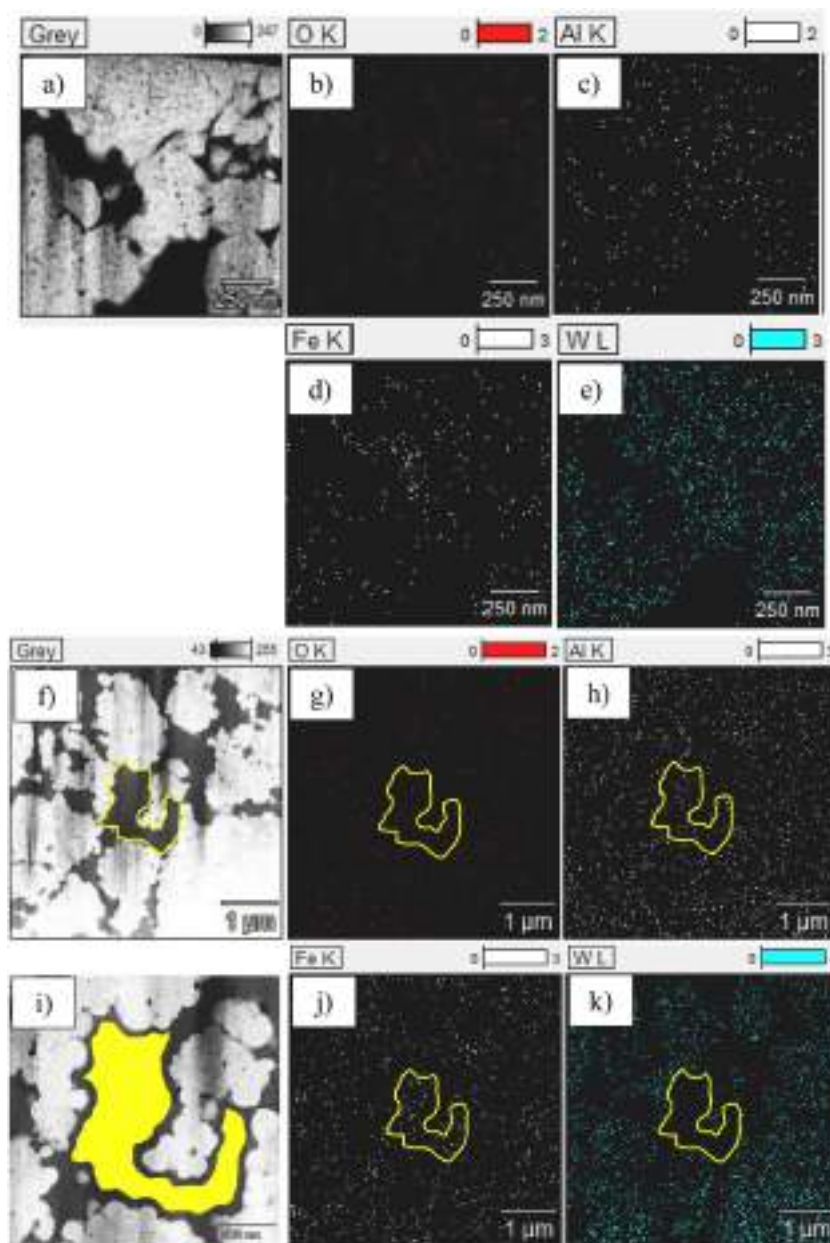
Fig. 9. Morphology (figures a), f), and i)) and chemical analysis (figures b)-e) and g)-k)) of various areas of $W_{90}Al_{10}$ (figures a)-e)) and $W_{80}Al_{20}$ (figures f)-k)) specimens sintered at 1000 °C. STEM and HAADF detector are used for imaging, thus the contrast is inverted in maps: Light regions are heavy (W) and dark regions are lighter (Al and Fe).

analysis shown in Fig. 5, although coarser structures are evident from TEM analysis. This is not surprising since the Rietveld method is more related to the XRD coherent domains (crystallites), which do not necessarily coincide with grains appearing in TEM micrographs [19].

Chemical analysis and the resulting estimated compositions from various areas of $W_{90}Al_{10}$ and $W_{80}Al_{20}$ specimens sintered at 1000 °C are shown in Fig. 9. Maps are performed using the STEM and HAADF detector for imagin; thus, the contrast is inverted: light regions are heavy (W-rich) and dark ones are lighter (Al- or Fe-rich). The quantitative analysis performed via EDX confirms the introduction of Fe during the ball milling process. Traces of other elements are identified but, since their contribution is negligible, they are omitted from the calculation. The oxygen concentration agrees with that is expected for this type of sample and preparation method, and no significant oxides formation has been observed.

$W_{90}Al_{10}$ and $W_{80}Al_{20}$ samples show large clusters of W-rich grains

where the Al content is about 14 at.% and 30 at.%, respectively. The relative amount of iron of about 10 at.% is similar for both samples. It is worth mentioning that Fe-rich areas were not found throughout the samples. This finding allows concluding that Fe is mostly dissolved in the W BCC lattice along with aluminum. However, some inter-cluster regions (yellow area in Figs. 9f) and i)), which are composed of Al and Fe in a ratio of about 1.2:1, appear in the $W_{80}Al_{20}$ sample. The formation of these areas may be the result of precipitating Fe-Al intermetallics, whose formation during the sintering process is induced in regions where localized high concentrations of Al and Fe are present.

Nanostructural details of the $W_{90}Al_{10}$ sample consolidated at 1000 °C are reported in Fig. 10. TEM micrographs show atomically Al-rich (dark) areas dispersed in the W-richer matrix. Some intergranular nanosized pores can also be observed in Fig. 10a). Dark regions are situated at the GBs (cf. Fig. 10b)), as well as in the grain interiors (cf. Fig. 10c)): the areas of the former are larger than the latter. Fig. 10d)
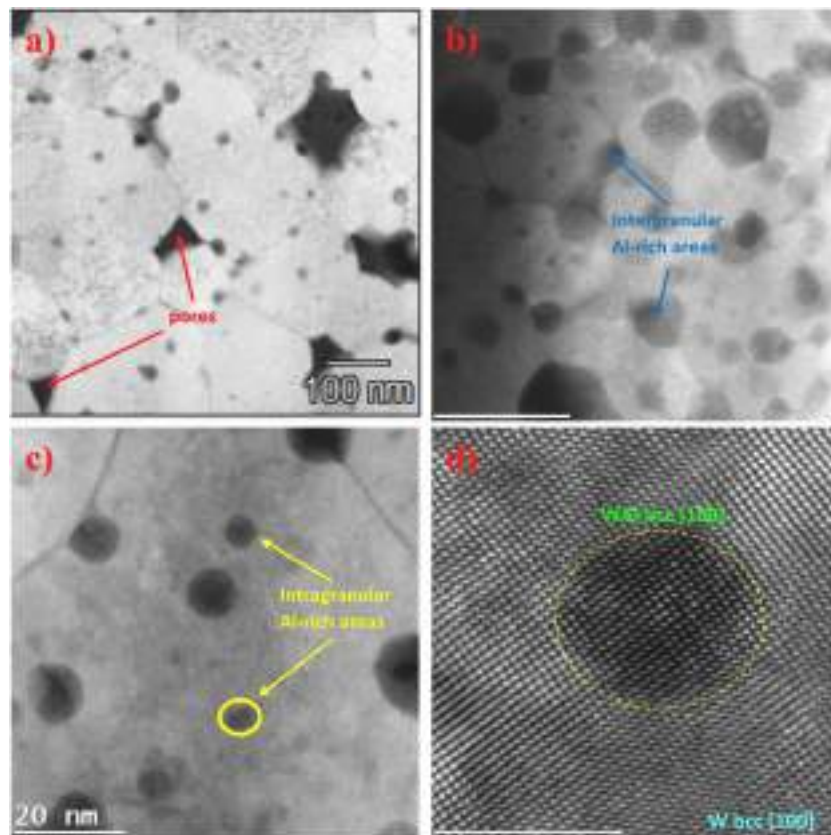
Fig. 10. Nanostructural details at various magnification of the $W_{90}Al_{10}$ sample consolidated at 1000 °C.
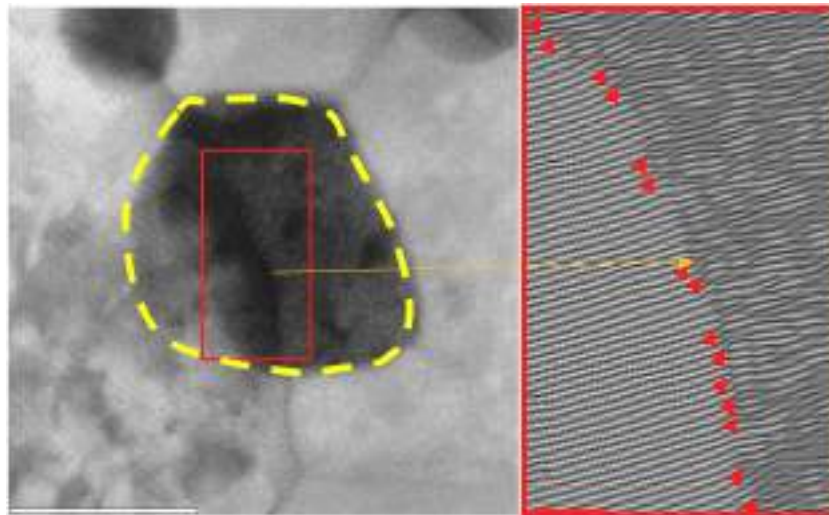

Fig. 11. High resolution TEM micrograph of a large Al-rich W alloy island located at a 3-way grain boundary in the $W_{90}Al_{10}$ sample consolidated at 1000 °C. The high defect density is highlighted in the reconstructed FFT image on the right side of the Figure.

shows a higher magnification of one of the dark areas sited inside the grains, which is about 5 nm in diameter. This area shows the same crystallographic structure of the host unit cell (W) with no discontinuity or misorientation (e.g., boundary) observed between the two regions.

More insights can be gained from Fig. 11, where high-resolution TEM shows the nanostructure of a large island located at the boundary between three grains. The chemical map of the dashed yellow contoured area appearing in Fig. 11a) is reported in Table 1. It reveals that dark regions are not characterized by the presence of Fe or other contaminants coming from the milling media or the sintering tools. Rather, the chemical analysis indicates that W and Al are present in a ratio of 1:1. This means that the Al content in the dark regions is significantly higher than that in the grain interior, which shows a W:Al ratio close to as prepared alloy stoichiometry (i.e., 4:1). Moreover, Fig. 11b shows the reconstructed Fourier transform (FFT) of a large Al-segregated region located at GB.

It is worth noting that the formation of W-Al intermetallic compounds at GBs can be ruled out. SAED of segregated regions, which can

Table 1
Chemical analysis of the dash yellow contoured area appearing in Fig. 11a).

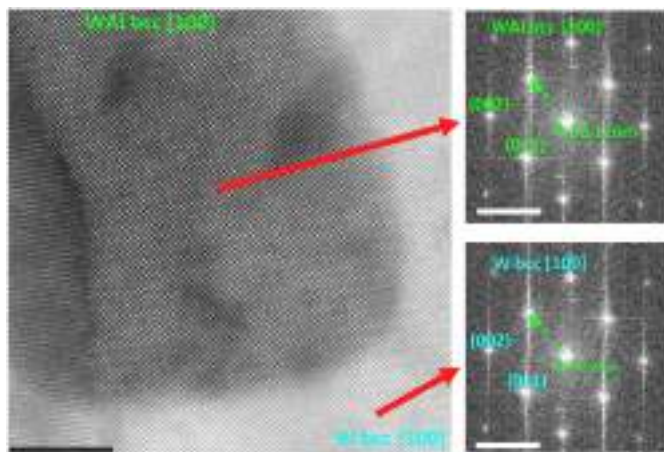| Element (line)	Wt%	Error	At. %	Error
N (K)	1.94	± 0.39	10.86	± 2.17
O (K)	3.88	± 0.30	18.99	± 1.45
Al (K)	12.11	± 0.37	35.17	± 1.08
W (N)	–	–	–	–
W (M)	–	–	–	–
W (L)	82.07	± 1.41	34.98	± 0.61
Total	100.00		100.00	

Fig. 12. Selected area electron diffraction (SAED) of segregated (dark) and grain interior (light) areas.

be found in Fig. 12, reveals only reflection planes characteristic of the BCC lattice. Furthermore, lattice parameters near GBs are slightly larger compared to those observed in the grain interior. Such volume increase of the W lattice can be reasonably ascribed to the higher concentration of Al atoms, which have a larger atomic volume than W. It is interesting to note that, according to the compositional range investigated in this work and the W-Al phase diagram [18], the formation of the intermetallics WAl_4 is thermodynamically favored. However, W-Al intermetallics show complex crystal structures [18]. Therefore, the energy penalty resulting from the misfit interface between the precipitating intermetallic phases and the BCC W-Al matrix makes this phenomenon unfavorable or kinetically hindered. Moreover, aluminum segregation at GBs may also contribute to stabilize the W-Al supersaturated solid solution thermodynamically with respect to intermetallic formation [7,20].

Fig. 13 confirms the presence of nanometer-sized Al-rich areas within the W-based structure. Different shapes of these regions can be observed. Specifically, Al-enriched particle-like islands are located at GBs and in the grain interiors (cf. Fig. 13a). The characteristic size of these areas is up to 20–30 nm. Aluminum-rich layers at GBs, characterized by a constant thickness of about 2–3 nm, can also be observed. Fig. 13b) shows details of an Al-rich region located at the triple junction (cf. red square in Fig. 13a)). The higher magnification of the island indicated in Fig. 13a (yellow square) is shown in Fig. 13c. It is worth noting that the upper part of this island is in contact with the grain boundary (blue arrow), while the lower part merges with the grain interior (green arrow). Misorientation at the GB and a certain degree of the disorder can be observed here. Instead, the lower portion of the Al-rich island shows a coherent interface with the W-rich matrix. Figs. 13d) focused on other Al-rich region located at the GBs (green square in Fig. 13a)). It appears that Al enrichment involves more than one atomic layer. In addition, areas showing some degree of disorder also characterize these regions.

It can be useful to compare the obtained results with similar findings

recently reported for thin films of W-Ti alloy [21]. Similarly, in this latter study, Ti-rich regions were found to be located at GBs as well as in the columnar grain interiors. The classical nucleation and growth process was considered for explaining the formation of Ti-rich regions at GBs because of the energetically more favorable conditions [21]. The presence of Ti-rich domains inside the grains was explained by the formation of the BCC Ti phase. Indeed, the cubic structure of such a phase was assumed to be stabilized by the coherency of the interface with the BCC W(Ti) solution phase and the limited solubility of W in Ti [21].

Although, as illustrated above, W-Al and W-Ti systems show common nanostructural features, they are different from the thermodynamic point of view. Specifically, the equilibrium phase diagram of W-Ti shows a large miscibility gap with a critical temperature of about 1470 K [22]. On the contrary, W and Al are characterized by a negative enthalpy of mixing with several intermetallic phases appearing in the corresponding phase diagram [18]. Therefore, while precipitation of BCC Ti-rich secondary phase in W-Ti alloys can be induced by supersaturation conditions, the latter cannot explain the formation of the Al-rich regions observed in this work. Indeed, the analysis reported in Figs. 10 and 12 already excluded the precipitation of FCC Al and intermetallic phases.

The findings related to the W-Al system can be better explained by considering GB segregation phenomenon [7,23]. Although experimental data are not yet available, a negative enthalpy of segregation of about −44.5 *kJ/mol* has been recently estimated [7]. Accordingly, segregation of Al to GBs is expected to occur, thus confirmed by the experimental results reported in this work. This is because Al enrichment may reduce the energy penalty associated with the GBs. However, it should also be noted that Al-rich areas are not uniformly distributed along the grain boundaries. This indicates that other factors may also contribute to the formation of these large W-depleted regions.

In particular, as shown in Fig. 11b, a multitude of point defects and mismatched atomic planes are identified along the interface. Then, it can be hypothesized that lattice strain and low local electronic density caused by defects may create preferential sites for the migration of Al atoms toward the interface. Large Al-segregated areas at GBs (cf. Fig. 10) may also be an effect of the elastic or structural strain therein released. The latter can then be the driving force that guides solute segregation toward the specific sites at GBs [24]. The same considerations can be invoked to explain the Al-rich zones observed in grain interiors (cf. Fig. 10). In fact, local defects (e.g., dislocations) can act as preferential sites for Al atoms segregation.

3.3. Mechanical testing

Fig. 14 reports the elastic modulus E of samples sintered at 1100 °C and evaluated through nanoindentation. For comparison purposes, the same property of fully dense W-Al alloys is also shown (red line). This was calculated according to a rule-of-mixture recently proposed [25] using the reference values of elastic modulus and density of pure tungsten and aluminum, i.e., $E_W^0 = 411$ *GPa*; $E_{Al}^0 = 70$ *GPa*; $\rho_W^0 = 19.25$ *Mg/m³*; $\rho_{Al}^0 = 2.7$ *Mg/m³*. It can be clearly seen that the measured values are lower than the expected ones for fully dense alloys, as an effect of the residual porosity of the consolidated samples (cf. Fig. 1). The dependence of the elastic modulus upon material porosity can be quantified by the following relation [26]:

$$E = E^0 \left(\frac{\rho}{\rho^0} \right)^a \tag{1}$$

where E^0 is the full density elastic modulus, ρ the sintered sample density, and ρ^0 the theoretical density of the alloys that can be calculated by means of the rule-of-mixture reported by Shaikh et al. [25]. The exponent a varies from 0.3 to 4, reflecting a sensitivity to the pore structure [26]. Green bars in Fig. 14 represent, for each alloy formulation, the expected values of the elastic modulus according to Eq. (1), where the measured relative densities are inserted, and by considering the
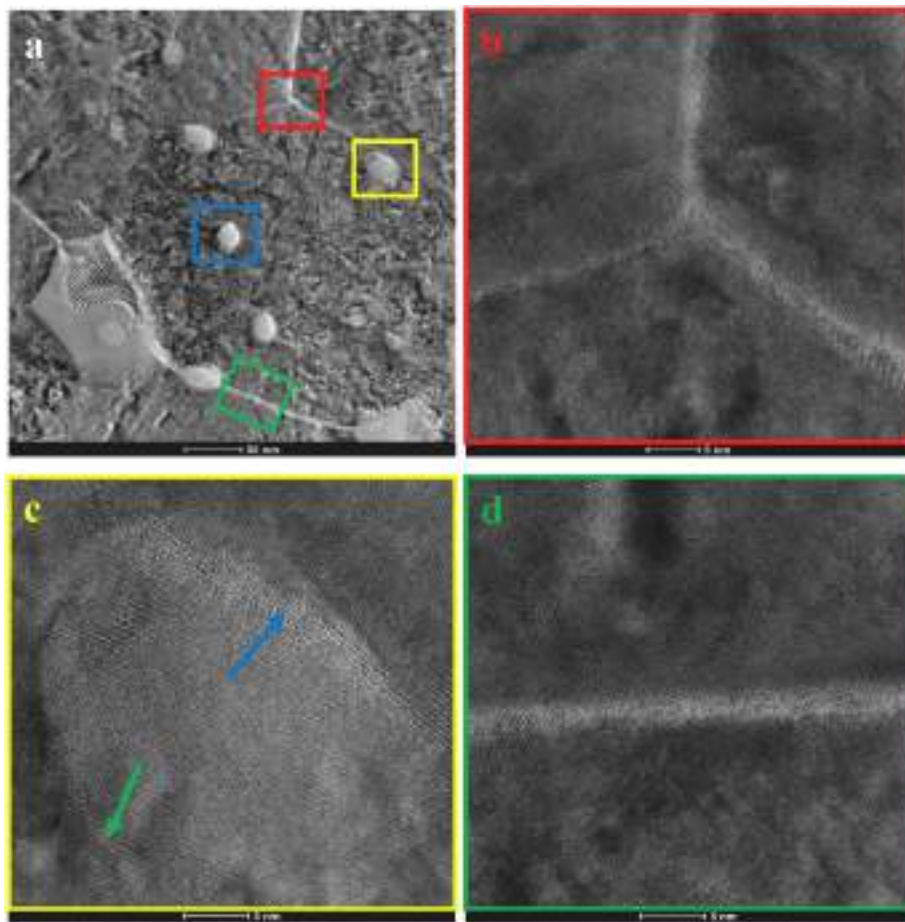
Fig. 13. a) High-resolution TEM of nanometer-sized Al-rich areas within the grain interior and at the grain boundaries in the $W_{80}Al_{20}$ sample consolidated at 1000 °C. Magnification of the areas contoured in figure a) by the red, yellow, and green boxes are shown in figures b), c) and d), respectively. (For interpretation of the references to colour in this figure legend, the reader is referred to the web version of this article.)
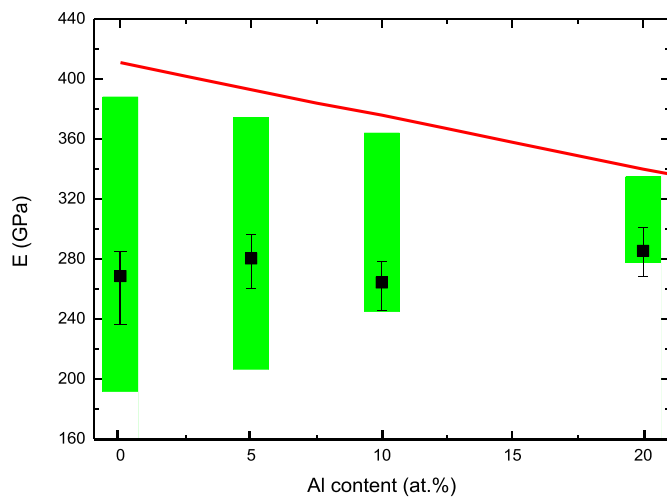

Fig. 14. Elastic modulus of W-Al alloys sintered at 1100 °C as a function of Al content. Red line gives the elastic modulus of fully dense alloys estimated according to the rule of mixing given by Shaikh et al. [25]. Green areas represent the estimated elastic modulus of porous alloys according to Eq. (1) by taking into account the uncertainty of paramater *c*. Samples porosity used in the calculation is reported in Fig. 1. (For interpretation of the references to colour in this figure legend, the reader is referred to the web version of this article.)
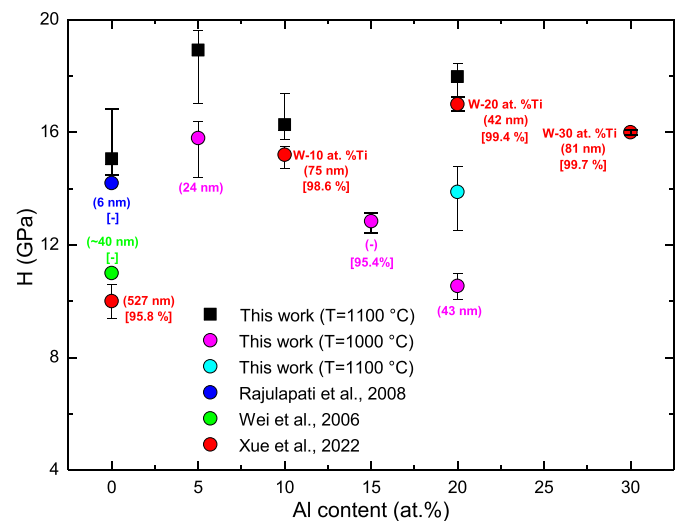

Fig. 15. Nanohardness (squares) and microhardness (circles) of W-Al alloys as a function of Al content. Literature data related to W-Ti alloys are also reported for the sake of comparison. For each datum, the corresponding grain size and sample relative density are reported in round and square brackets, respectively. Complementary data for the sample fabricated in this work are reported in Figs. 1 and 5.

variability of coefficient *a*. A good agreement between experimental data and the estimated values can be clearly observed.

The hardness of samples sintered at 1000 °C and 1100 °C was also measured. Fig. 15 shows nano- (black squares) and micro- (magenta and cyan circles) hardness of SPSed samples with different Al content. Micro-hardness values taken from the literature (green, blue, and red circles) are also reported for nanocrystalline or ultrafine pure tungsten [27,28] and W-Ti alloys [29]. When available, for each data point, the related grain size and sample relative density are reported in round and square brackets, respectively. The reader can refer to Figs. 1 and 5 for the complementary data of samples fabricated in this work.

Fig. 15 is intended to give an overview of the order of magnitude of hardness that can characterize W and W-alloys with a structure in the nano- or submicro-meter range. A direct comparison is instead not straightforward since hardness is affected by sample density and grain size along with the alloy composition. In the case of nanoindentation, additional factors such as the well-known indentation size effect (ISE) [30], or tips [31] and strain rate [32] influence should be considered to ascertain the actual material hardness.

However, some qualitative insights can be obtained by analyzing the results reported in Fig. 15. First, it should be noted that the hardness values of the W-Al alloy obtained in this work are higher than those reported in the literature for coarse- or submicro-grained pure tungsten [33–35]. This result can be ascribed to the nanostructure that characterizes the produced alloys (cf. Figs. 5 and 8), and it agrees with the well-known Hall-Petch effect. Fig. 15 shows as well that that nano-hardness is higher than microindentation outputs. This is somehow expected due to the several factors affecting the hardness evaluation through nano-indentation [36]. It is also worth noting that the hardness of W-Al alloys compared very well with literature data recently reported for W-Ti alloys [29].

Fig. 15 does not show a clear correlation between hardness and Al content. This finding may be a consequence of the different homologous temperatures experienced by each alloy during SPS. This, in turn, could result in a diverse sintering and grain growth evolution as the aluminum content is varied. On the one hand, at low homologous temperature (low Al content), the negative impact on hardness caused by the high residual porosity is counterbalanced by the beneficial effect of limited grain growth and the resulting fine microstructure. On the other hand, the positive effect of a higher relative density on hardness is compensated by the decremental influence of the coarser grain size obtained when the homologous temperature increases (i.e., high Al content).

4. Conclusions

Single-phase nanocrystalline $W_{100-x}Al_x$ (x = 0–20 at.%) powders were prepared by MA and consolidated by SPS at 1000–1100 °C. Alloying W with Al significantly improves the sinterability of powders and allows obtaining dense samples (up to 96% of relative density). Sintered samples consist of a homogeneous, chemically disordered W-based BCC nanocrystalline solid solution with the same chemical composition as the initial powder mixture. Neither W-Al intermetallic compounds nor free elemental Al have been detected.

The average crystallite size of consolidated samples remains well below 100 nm for all the samples, and down to about 25 nm for the $W_{95}Al_5$ Alloy composition. The grain size undergoes a non-monotonic variation with the Al content due to the competition between grain growth and GB segregation processes. As the Al content increases, the stabilization effect of Al segregation at GBs exceeds the faster grain growth caused by the higher homologous temperature. Conversely, GB segregation of Al can only slow down grain growth as the homologous temperature becomes higher at larger Al contents.

The homogeneous W-Al alloy is spotted with nanometer-sized Al-rich areas of different shape. Regions richer in Al of about 20–30 nm are also present at both GBs and grain interior. Al-rich layers at GBs with a thickness of about 2–3 nm can be also observed.

Consolidated W-Al exhibits room-temperature nanohardness of 18–19.5 GPa and Vickers hardness up to 16 GPa, values definitely larger than those of coarse- or submicron-grained pure W. The high hardness of consolidated W-Al alloys can be reasonably ascribed to the nano-structure retention induced by the GB segregation of Al.

Declaration of Competing Interest

The authors declare that they have no conflict of interest.

Data availability

Data will be made available on request.

References

[1] U. Abdullah, M. Ali, E. Pervaiz, R. Khosa, An inclusive perspective on the recent development of tungsten-based catalysts for overall water-splitting: a review, Int. J. Energy Res. 46 (8) (2022) 10228–10258.

[2] R.M. German, Lower sintering temperature tungsten alloys for space research, Int. J. Refract. Met. Hard Mater. 53 (2015) 74–79.

[3] S. Ke, X. Min, Y. Liu, R. Mi, X. Wu, Z. Huang, M. Fang, Tungsten-based nanocatalysts: research progress and future prospects, Molecules 27 (2022) 4751.

[4] S. Omole, A. Lunt, S. Kirk, A. Shokrani, Advanced processing and machining of tungsten and its alloys, J. Manufact. Mater. Process. 6 (1) (2022) art. no. 15.

[5] Y. Wu, Manufacturing of tungsten and tungsten composites for fusion application via different routes, Tungsten 1 (1) (2019) 80–90.

[6] H. Xu, L.-L. He, Y.-F. Pei, C.-Z. Jiang, W.-Q. Li, X.-H. Xiao, Recent progress of radiation response in nanostructured tungsten for nuclear application, Tungsten 3 (1) (2021) 20–37.

[7] F. Torre, C. Mingazzini, D.M. Gattia, T. Huminiuc, A. Rinaldi, T. Polcar, F. Delogu, A.M. Locci, Investigation on the thermodynamic stability of nanocrystalline W-based alloys: A combined theoretical and experimental approach, Materials 14 (23) (2021) art. no. 7179.

[8] Y. Ouyang, X. Zhong, W. Wu, Extended solid solubility for Al-W binary system by mechanical alloying, Sci China Ser A Math Phys Astron 43 (2) (2000) 180–184.

[9] H.G. Tang, X.F. Ma, W. Zhao, X.W. Yan, R.J. Hong, Preparation of W-Al alloys by mechanical alloying, J. Alloys Compd. 347 (1–2) (2002) 228–230.

[10] M. Rafiei, S. Khademzadeh, N. Parvin, Characterization and formation mechanism of nanocrystalline W-Al alloy prepared by mechanical alloying, J. Alloys Compd. 489 (1) (2010) 224–227.

[11] F. Torre, T. Huminiuc, E. Musu, T. Polcar, F. Delogu, A.M. Locci, Fabrication of nanocrystalline supersaturated W–Al alloys with enhanced thermal stability and high sinterability, J. Phys. Chem. Solids 148 (2021) art. no. 109686.

[12] C.J. Zhu, X.F. Ma, W. Zhao, H.G. Tang, J.M. Yan, S.G. Cai, Processing, microstructure and mechanical properties of W50Al50 bulk alloy obtained by mechanical alloying and hot-pressing, Scr. Mater. 51 (10) (2004) 993–997.

[13] C.J. Zhu, X.F. Ma, W. Zhao, H.G. Tang, J.M. Yan, S.G. Cai, Synthesis, microstructure and mechanical properties of Al40W60 bulk alloy obtained by mechanical alloying and hot-pressing, Adv. Eng. Mater. 7 (4) (2005) 256–260.

[14] L. Lutterotti, H. Pillière, C. Fontugne, P. Boullay, D. Chateigner, Full-profile search–match by the Rietveld method, J. Appl. Crystallogr. 52 (3) (2019) 587–598.

[15] W.C. Oliver, G.M. Pharr, An improved technique for determining hardness and elastic modulus using load and displacement sensing indentation experiments, J. Mater. Res. 7 (6) (1992) 1564–1583.

[16] M. Biesuz, V.M. Sglavo, Liquid phase flash sintering in magnesia silicate glass-containing alumina, J. Eur. Ceram. Soc. 37 (2) (2017) 705–713.

[17] V. Zamora, F. Guiberteau, O. Borrero-López, A.L. Ortiz, Spark plasma sintering and dry sliding-wear of ZrC-16.7 vol.% Co cemented carbides, Ceram. Int. 47 (9) (2021) 12803–12811.

[18] I. Ansara, A.T. Dinsdale, M.H. Rand, COST 507: Thermochemical Database for Light Metal Alloys vol. 2, 1998.

[19] T. Ungár, G. Tichy, J. Gubicza, R.J. Hellmig, Correlation between subgrains and coherently scattering domains, Powder Diffract. 20 (4) (2005) 366–375.

[20] A.M. Locci, Theoretical assessment of thermodynamic stability in nanocrystalline metallic alloys, Materials 12 (20) (2019) 3408.

[21] M. Callisti, F.D. Tichelaar, T. Polcar, In situ TEM observations on the structural evolution of a nanocrystalline W-Ti alloy at elevated temperatures, J. Alloys Compd. 749 (2018) 1000–1008.

[22] S. Jonsson, Reevaluation of the Ti-W system and prediction of the Ti-W-N phase diagram, Zeitschrift fuer Metallkunde/Mater. Res. Adv. Techn. 87 (10) (1996) 784–787.

[23] J. Weissmüller, Alloy effect in nanostructures, Nanostruct. Mater. 3 (1993) 261–272.

[24] A.R. Miedema, Surface segregation in alloys of transition metals, Zeitschrift fuer Metallkunde/Mater. Res. Adv. Techn. 69 (7) (1978) 455–461.

[25] S.M. Shaikh, V.S. Hariharan, S.K. Yadav, B.S. Murty, CALPHAD and rule-of-mixtures: a comparative study for refractory high entropy alloys, Intermetallics 127 (2020) art. no. 106926.

[26] R.M. German, Power Metallurgy Science, Metal Powder Industries Federation, Princeton, New Jersey, USA, 1994.

[27] Q. Wei, H.T. Zhang, B.E. Schuster, K.T. Ramesh, R.Z. Valiev, L.J. Kecskes, R. J. Dowding, L. Magness, K. Cho, Microstructure and mechanical properties of super-strong nanocrystalline tungsten processed by high-pressure torsion, Acta Mater. 54 (2022) 4079–4089.

[28] K.V. Rajulapati, R.O. Scattergood, K.L. Murty, Z. Horita, T.G. Langdon, C.C. Koch, Mechanical properties of bulk nanocrystalline aluminum-tungsten alloys, Metall. Mater. Trans. A 39 (2008) 2528–2534.

[29] H.X. Xue, X.C. Cai, B.R. Sun, X. Shen, C.C. Du, X.J. Wang, T.T. Yang, S.W. Xin, Bulk nanocrystalline W-Ti alloys with exceptional mechanical properties and thermal stability, J. Mater. Sci. Technol. 114 (2022) 16–28.

[30] D. Faghihi, G.Z. Voyiadjis, Determination of nanoindentation size effects and variable material intrinsic length scale for body-centered cubic metals, Mech. Mater. 44 (2012) 189–211.

[31] N.I. Tymiak, D.E. Kramer, D.F. Bahr, T.J. Wyrobek, W.W. Gerberich, Plastic strain and strain gradients at very small indentation depths, Acta Mater. 49 (2001) 1021–1034.

[32] P.S. Phani, W.C. Oliver, Ultra high strain rate nanoindentation testing, Materials 10 (2017) 663.

[33] T.S. Srivatsan, K. Manigandan, M. Petraroli, R.M. Trejo, T.S. Sudarshan, Influence of size of nanoparticles and plasma pressure compaction on microstructural development and hardness of bulk tungsten samples, Adv. Powder Technol. 24 (1) (2013) 190–199.

[34] A. Leitner, V. Maier-Kiener, D. Kiener, Extraction of flow behavior and Hall–Petch parameters using a nanoindentation multiple sharp tip approach, Adv. Eng. Mater. 19 (4) (2017) art. no. 1600669.

[35] T.-X. Li, J.-W. Miao, E.-Y. Guo, H. Huang, J. Wang, Y.-P. Lu, T.-M. Wang, Z.-Q. Cao, T.-J. Li, Tungsten-containing high-entropy alloys: a focused review of manufacturing routes, phase selection, mechanical properties, and irradiation resistance properties, Tungsten 3 (2) (2021) 181–196.

[36] L. Qian, M. Li, Z. Zhou, H. Yang, X. Shi, Comparison of nano-indentation hardness to microhardness, Surf. Coat. Technol. 195 (2–3) (2005) 264–271.